

## Periodic and Phase-locked Modulation in PSR B1929+10 Observed with FAST

F. F. KOU,<sup>1,2</sup> W. M. YAN,<sup>2,3</sup> B. PENG,<sup>1</sup> J. G. LU,<sup>1</sup> K. LIU,<sup>4,1</sup> C. M. ZHANG,<sup>1</sup> R. G. STROM,<sup>5,6</sup> L. WANG,<sup>1,7,8</sup>  
J. P. YUAN,<sup>2,9</sup> RAI YUEN,<sup>2,3</sup> Y. Z. YU,<sup>10</sup> J. M. YAO,<sup>1,2</sup> B. LIU,<sup>1</sup> J. YAN,<sup>1</sup> P. JIANG,<sup>1</sup> C. J. JIN,<sup>1</sup> D. LI,<sup>1,11</sup> L. QIAN,<sup>1</sup>  
Y. L. YUE,<sup>1</sup> Y. ZHU,<sup>1</sup> AND (THE FAST COLLABORATION)

<sup>1</sup>CAS Key Laboratory of FAST, National Astronomical Observatories, Chinese Academy of Sciences, Beijing 100101, P. R. China

<sup>2</sup>Xinjiang Astronomical Observatories, Chinese Academy of Sciences, Urumqi, 830011, P. R. China

<sup>3</sup>Key Laboratory of Radio Astronomy, Chinese Academy of Sciences

<sup>4</sup>Max-Planck-Institut für Radioastronomie, Auf dem Hügel 69, Bonn, D-53121, Germany

<sup>5</sup>ASTRON, Postbus 2, 7990 AA Dwingeloo, The Netherlands

<sup>6</sup>Astronomical Institute, University of Amsterdam, The Netherlands

<sup>7</sup>Jodrell Bank Centre for Astrophysics, School of Physics and Astronomy  
The University of Manchester Manchester, M13 9PL, UK

<sup>8</sup>School of Astronomy and Space Science, University of Chinese Academy of Sciences

<sup>9</sup>Department of Astronomy, China West Normal University, Nanchong 637009, P. R. China

<sup>10</sup>Qiannan Normal University for Nationalities, Duyun 558000, P. R. China

<sup>11</sup>NAOC-UKZN Computational Astrophysics Centre, University of KwaZulu-Natal, Durban 4000, South Africa

### ABSTRACT

We present a detailed single-pulse analysis for PSR B1929+10 based on observations with the Five-hundred-meter Aperture Spherical radio Telescope (FAST). The main pulse and interpulse are found to be modulated with a periodicity of  $\sim 12$  times the pulsar's rotational period ( $P$ ). The  $\sim 12P$  modulation is confirmed as a periodic amplitude modulation instead of systematic drifting. The periodic amplitude modulation in the IP is found to be anti-correlated with that in the weak preceding component of the MP (MP\_I), but correlated with that in the first two components of the MP (MP\_II), which implies that the modulation patterns in the IP and the MP are phase-locked. What is more interesting is that the modulation in MP\_II is delayed that in the IP by about  $1P$ . Furthermore, high sensitivity observations by FAST reveal that weak emission exists between the MP and the IP. In addition, we confirm that the separation between the IP and the MP is independent of radio frequency. The above results are a conundrum for pulsar theories and cannot be satisfactorily explained by the current pulsar models. Therefore, our results observed with FAST provide an opportunity to probe the structure of pulsar emission and the neutron star's magnetosphere.

*Keywords:* pulsars: general– stars: neutron– pulsars: individual (PSR B1929+10)

### 1. INTRODUCTION

To explore pulsar emission geometry and its magnetosphere, many observations and studies of PSR B1929+10 (PSR J1932+1059) have been performed because its integrated pulse profile clearly exhibits both a main pulse (MP) and an interpulse (IP) (Phillips 1990; Rankin & Rathnasree 1997), features usually thought to be pulsar emission from two opposite magnetic poles. PSR B1929+10 was discovered in the Molonglo survey by Large et al. (1968), shown to be a normal pulsar

with a characteristic age of  $\sim 3.1$  Myr, and recently it was also detected in the X-ray band (Becker et al. 2006; Misanovic et al. 2006). At radio frequencies, the phase separation between the MP and IP is about  $187.4 \pm 0.2^\circ$  and it is reported to be independent of observing frequency (Perry & Lyne 1985). Polarimetric studies have been carried out at various observing frequencies for this pulsar, showing it has high linear polarization and a very small circular component (Rankin & Rathnasree 1997). According to previous works, the magnetic inclination angle  $\alpha$  (the angle between the magnetic axis and the rotation axis), which can be derived by fitting the position-angle of the linear polarization to the rotating vector model (RVM for short), was measured to

be approximately  $35^\circ$  (Perry & Lyne 1985; Rankin & Rathnasree 1997; Stairs et al. 1999).

Fluctuation spectrum analysis showed that the pulsar’s emission is modulated periodically, with two significant peaks at 0.095 cycles/period (cpp) ( $11P$ ) and 0.1795 cpp ( $5.57P$ ), respectively (Backer 1973; Rankin & Rathnasree 1997). Two drifting features with different periods in opposite directions were found by Weltevrede et al. (2006) using the Westerbork Synthesis Radio Telescope (WSRT) in the Netherlands at wavelength 21 cm. However, Basu et al. (2016, 2019a) claimed that there is no systematic drifting but periodic amplitude fluctuation with a period of  $11.5 \pm 1.3P$  based on Giant Meterwave Radio Telescope (GMRT) observations at 333 MHz.

Weak emission between the MP and the IP was first detected by Perry & Lyne (1985), and was clearly identified at 430 MHz with the Arecibo 300 m telescope (Phillips 1990; Rankin & Rathnasree 1997). Because of the weak emission throughout most of its rotational period, PSR B1929+10 had been categorized in the group of single-pole interpulse pulsars, which means that the MP and the IP come from the same magnetic pole (Phillips 1990). However, a contradictory conclusion can be derived based on the pulse profile components. PSR B1929+10 was identified as a two-pole interpulse pulsar according to its core-emission dominated profile (Rankin & Rathnasree 1997; Basu et al. 2019b), which means that the MP and the IP come from the two opposite magnetic poles of the pulsar.

In this paper, to clearly present the emission properties of PSR B1929+10, we exploited the largest single dish telescope FAST to make single-pulse observations of this pulsar (Nan et al. 2011). The high sensitivity observations of PSR B1929+10 with FAST reveal previously unknown and more complex emission properties, which may further complicate our understanding of radio emission in this pulsar. In this paper, we investigate the modulation and interaction between the IP and the MP, and try to discuss the theoretical restrictions based on our results. In section 2, the observations and data processing method are introduced. The results are given in section 3. We summarize our results and discuss the possible geometric structure of the magnetosphere for PSR B1929+10 in sections 4 and 5, respectively.

## 2. OBSERVATIONS

FAST is located in Guizhou, China, with its whole aperture being 500 m and with an illuminated sub-aperture of 300 m during normal operation. A 19-beam receiver covering 1.05-1.45 GHz (the so called FLAN: (Li et al. 2018)) has been mounted for use since July 2018. It

contains a temperature stabilized noise injection system, with a noise signal injected from a single diode (Jiang et al. 2020). The collected data are captured by a digital backend based on Reconfigurable Open-architecture Computing Hardware–version2 (ROACH2) (Jiang et al. 2019, 2020), and are recorded in search-mode PSRFITS data format (Hotan et al. 2004), with time and frequency resolutions of  $49.152\mu\text{s}$  and 0.122 MHz, respectively.

The observations of PSR B1929+10 in this paper were performed on 2018 September 5 and 2019 November 22. A total of 1.5 hours of observations were recorded. More than 20,000 single pulses were obtained from these two observations. The data were processed to remove dispersion delay caused by the interstellar medium and produce single-pulse archives with the DSPSR software packages (van Straten & Bailes 2011). The ephemeris of the pulsar was obtained from the ATNF pulsar catalogue (PSRCAT, version 1.56) (Manchester et al. 2005). The channels with strong radio frequency interference (RFI) were removed using the PSRCHIVE packages (van Straten et al. 2010). A polarization calibration noise signal was injected at an off-source (pulsar) position and recorded before the pulsar observation on 2019 November 22. However, no stable radio flux density calibrator was observed at that time, and no polarization calibration data were recorded for the observation on 2018 September 5. We could only get a polarization pulse profile for the observation of 2019 November 22.

## 3. RESULTS

### 3.1. The single pulse modulation

The polarization profile for the observation on 2019 November 22 is shown in Fig. 1. The longitude of the MP’s pulse peak is set to be zero. The IP follows the MP by  $186.3 \pm 0.2^\circ$ , with peak intensity about 3% that of the MP at a central frequency of 1.25 GHz. A weak preceding component which is about  $20^\circ$  ahead of the MP peak can be identified (see the enlarged plot/bottom panel in Fig. 1). A single-pulse stack from 2019 November 22 is plotted in Fig. 2. The left and right columns show the single pulses of the MP and IP, respectively, for the same rotation of the pulsar. As shown in the right column of Fig. 2, it seems that the energy of the IP fluctuates between strong and weak states periodically. The left column shows that the preceding part of the MP has a clearer modulation than other parts of the MP. There is no obvious drifting feature found in the pulse stack.

To investigate the single pulse modulation in detail, we carried out an analysis of fluctuation spectra with the PSRSALSA packages for observations reported here, which contains the modulation index, the Longitude-Resolved Fluctuation Spectrum (LRFS) and the Two-

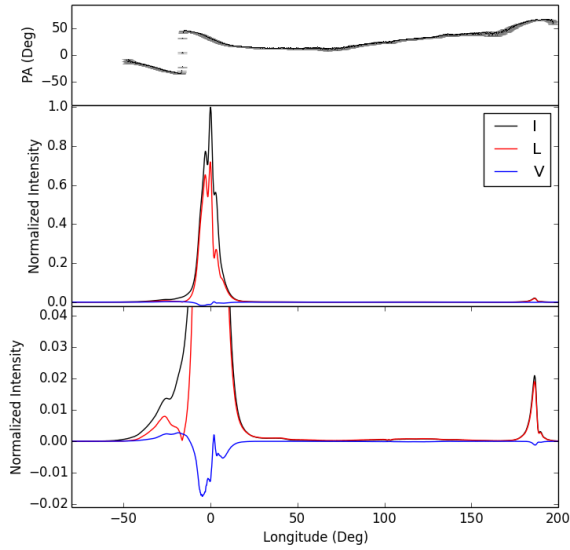


**Figure 1.** The mean pulse profile of PSR B1929+10 from the observation of 2019 November 22. The upper panel gives the position angles of the linearly polarized emission. The middle and bottom panels show the mean pulse profile for total intensity (black line), linearly polarized intensity (red line), and circularly polarized intensity (blue line). The bottom panel is the expanded plot of the middle panel.

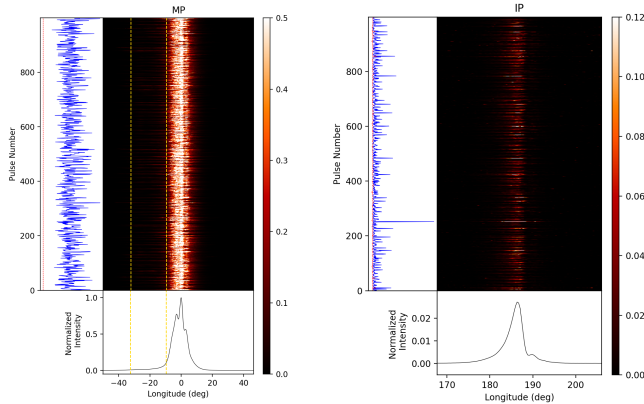


**Figure 2.** The single-pulse stack of PSR B1929+10 from the observation of 2019 November 22. The left and right columns show the longitude range around the MP and the IP for the same rotation, respectively. The two vertical dashed lines in the left column define the pulse longitudes of the preceding part of the MP. The left panel of each column shows the energy variations for the on-pulse range (blue solid line) and the off-pulse range (red dashed line). The bottom panels show the integrated pulse profiles which are normalized to the peak intensity of the MP .

Dimensional Fluctuation Spectrum (2DFS) (Edwards & Stappers 2002; Weltevrede et al. 2006). The modulation index is a measure of the factor of intensity variability from pulse to pulse (Weltevrede et al. 2006). The LRFS is used to detect the periodicity of the subpulse modulation. The 2DFS is to determine if the subpulses are drifting in pulse longitude. Here, we chose to plot the vertical axis of the LRFS and 2DFS in units of  $P/P_3$ , and the horizontal axis of the 2DFS in units of  $P/P_2$ , where  $P_3$  is the vertical drift band separation and  $P_2$  is the horizontal drift band separation.

Fig. 3 shows fluctuation spectra analyses of PSR B1929+10 based on the observation of 2019 November 22. As shown in the top windows of Fig. 3, the modulation indices of the IP and the weak preceding component of the MP are much higher than those of other components. Correspondingly, the spectral analysis of the IP shows clear intensity modulation and identifiable periodicity. Meanwhile, the spectra of the MP have broad low-frequency features ( $0.04 \sim 0.22$  cpp), mainly from the trailing parts. There are two relatively significant features from the preceding part of the MP, with peaks around 0.1 cpp and 0.18 cpp, which are roughly consistent with the results of Backer (1973). Weltevrede et al. (2006) reported two oppositely drifting features with different  $P_3$  values, and they indicated that those structures arose from the leading half of the MP. However, the 2DFS (bottom windows of Fig. 3) shows no obvious horizontal feature, which indicates that there is no systematic drifting but only periodic amplitude fluctuation in our data.

The time varying LRFS was used to check the stability of the fluctuation (Basu et al. 2016). This was done by calculating the LRFS for each 256-pulse block of the entire observation by shifting the starting point by 50 periods. In order to avoid being affected by the relatively strong MP emission, the spectrum of its weak preceding component (MP\_I), from  $-45^\circ$  to  $-16^\circ$ , was analysed separately. The time variation of the LRFS of the IP and the weak preceding component is shown in the bottom row of Fig. 4. From the average LRFS, the peak frequency  $f_p$  and the corresponding error  $\delta f_p$  could be determined (Basu et al. 2016). It is  $0.086 \pm 0.014$  cpp for the IP and  $0.086 \pm 0.018$  cpp for the weak preceding component, which implies a modulation period of  $P_3 \sim 12P$  for both the IP and the weak preceding components. Our results are consistent with those of Basu et al. (2016) who used GMRT data at 333 MHz. This implies that the fluctuation features could be independent of frequency.

### 3.2. The Phase Locking

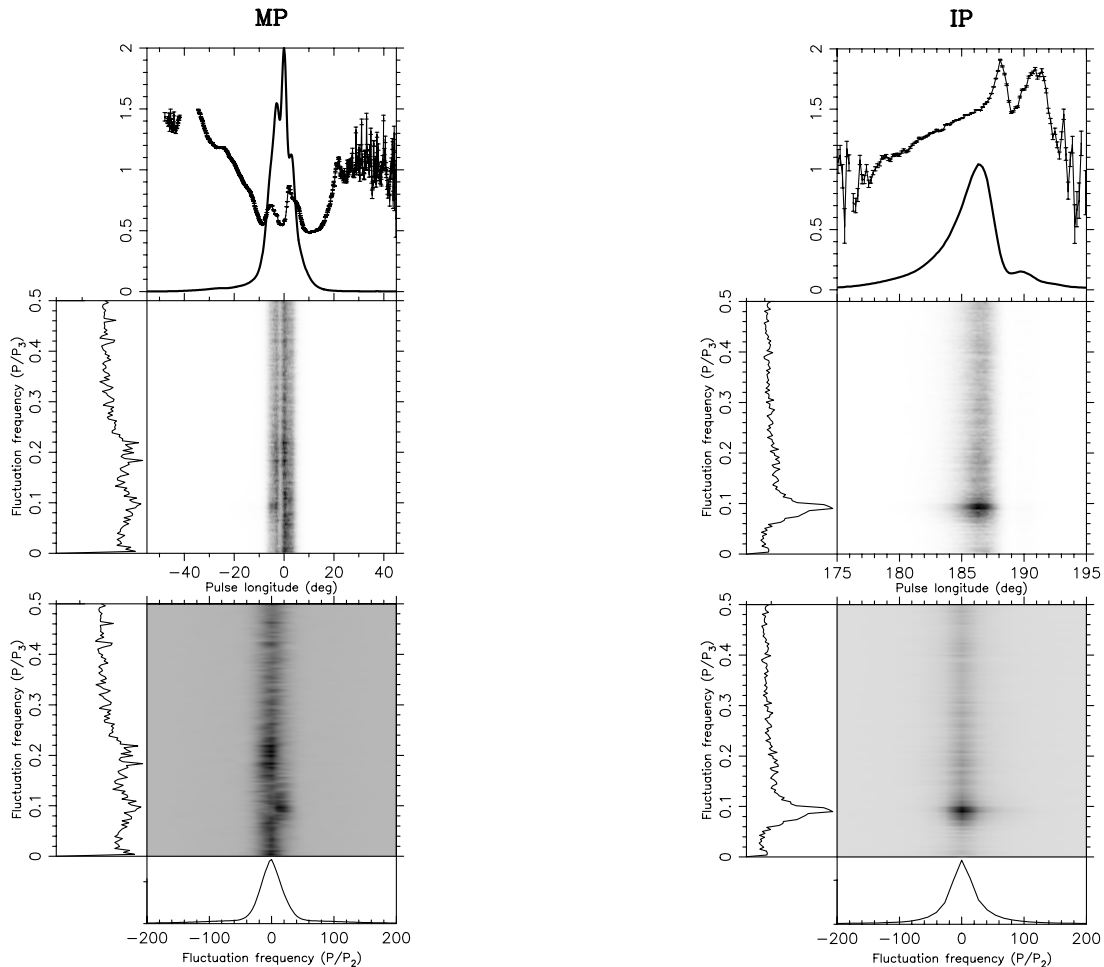


**Figure 3.** The fluctuation spectral analysis of PSR B1929+10 for the observation of 2019 November 22. The left column is the fluctuation spectrum of the MP for the first 256 pulses, and the right column is that of the IP. The top panels of each column show the longitude-resolved modulation index and the mean pulse profile. The intensities of the MP and the IP are scaled by 2 times and 50 times, respectively. The middle and bottom panels are the LRFS and 2DFS, respectively.

Since the IP and the weak preceding component of the MP show similar periodic fluctuations, we explore the phase connection between them in this subsection. The longitude-longitude correlation between the MP (from  $-57^\circ$  to  $34^\circ$ ) and the IP (from  $164^\circ$  to  $210^\circ$ ) at zero delay is shown in Fig. 5. The square regions on the diagonal are the autocorrelations for the MP and the IP. The rectangles on the top-left and bottom-right are the cross correlation regions between the MP and the IP. The region is largely negative for the correlation (blue) between the IP and the weak preceding component of the MP, but weakly positive (red) for the correlation between the IP and the first two components of the MP. This means that the emission in IP is anti-correlated with that of the weak preceding component of the MP, but correlated with that of the first two components of the MP. As discussed in subsection 3.1, there are also two relatively significant modulation features in the first two components of the MP with peaks around 0.1 cpp

and 0.18 cpp (the left column of Fig. 3). The correlation diagram indicates that the pulse longitudes with the same modulation period are locked.

According to the correlation diagram, the longitudes of the MP with negative correlation correspond to the weak preceding component (MP\_I). The regions with positive correlation correspond to the first two components (from  $-15^\circ$  to  $2^\circ$ ), and called MP\_II. The cross-correlations between the pulse energies of the IP and parts of the MP are shown in Fig. 6. It can be seen that the cross-correlation reaches its maximum value of  $-0.37$  at zero lag (the solid line). This means that the pulse energy modulation of the IP is anti-correlated with that of the MP\_I, which is called phase-locked modulation. Furthermore, the  $\sim 12P$  modulation feature in the IP and the MP\_I is also clearly detected from the cross-correlation function. Contrary to the negative correlation between the IP and the MP\_I, the energy variation of the IP is positively correlated with that of the MP\_II

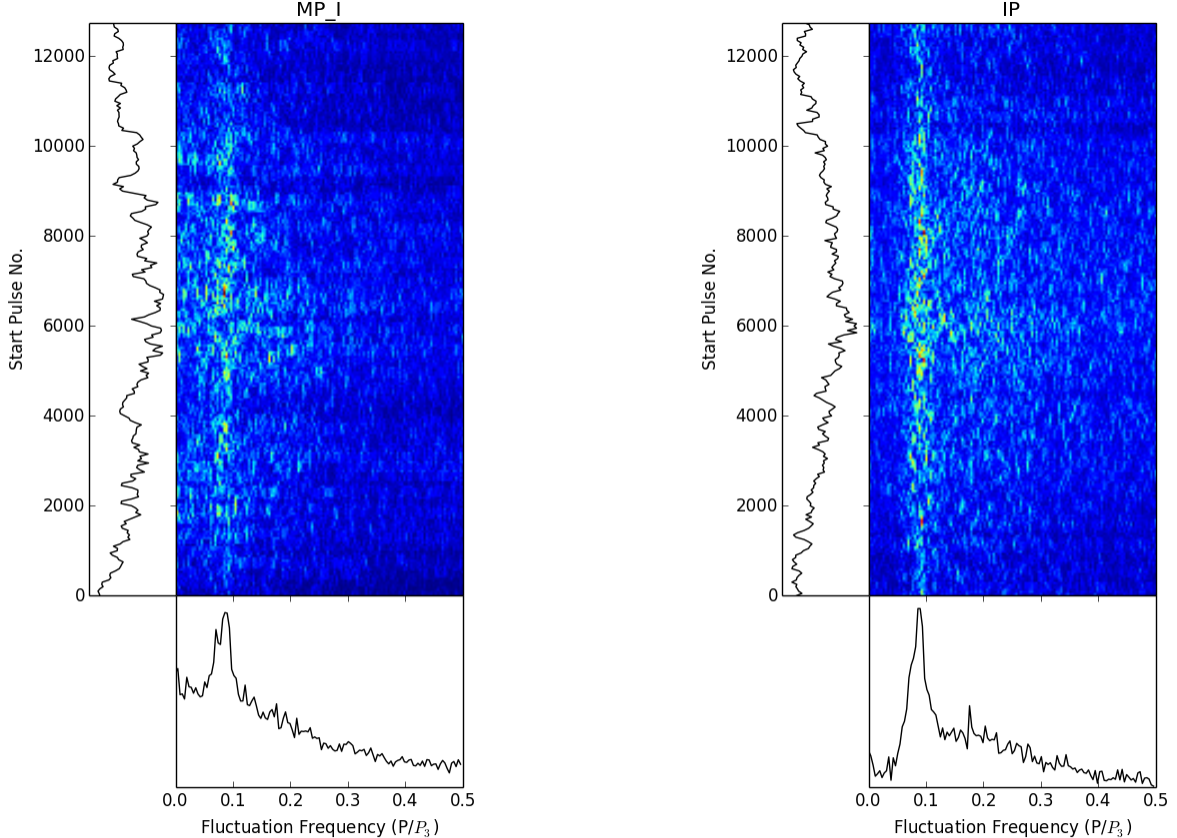


**Figure 4.** The time varying LRFs of the weak preceding component of the MP (left column, labeled as MP\_I) and the IP (right column). The side panel of each column shows the temporal variation of the LRFs, and the bottom panel is the average LRFs.

(the dashed line in Fig. 6). The peak of the correlation function is about 0.45. We notice that the peak of the correlation function is offset from zero lag, which corresponds to a delay of  $\sim 1P$ . This is referred to as a phase-locked delay (Weltevrede et al. 2012).

We carried out further analysis of the phase variation to study the  $\sim 12P$  modulation in detail, which is shown in Fig. 7. Based on the time varying LRFs, the fluctuation spectra with strongest  $\sim 12P$  modulation were selected<sup>1</sup>. The spectral amplitudes at the frequency of the  $\sim 12P$  modulation were calculated and averaged in each pulse bin. The amplitudes and their averaged values are shown as red points and black points in the top panels of Fig. 7, respectively. The corresponding phase variations were also estimated. To avoid arbitrary phase differences between different blocks of LRFs, the phase

<sup>1</sup> The fluctuation spectra value at the frequency corresponding to the  $\sim 12P$  modulation is 3 times larger than the rms level of the baseline.

at the pulse longitude of the IP's peak intensity was set to be zero, and the phase differences across the pulse window were estimated. The phase differences and their averages at a given phase longitude are plotted as red points and black points in the middle panels of Fig. 7, respectively. As shown in the right column of Fig. 7, the amplitudes during the on-pulse range of the IP change consistently, and the corresponding phase differences are close to  $0^\circ$ . This confirms that the whole IP is modulated by the same period ( $\sim 12P$ ). Moreover, there is no significant drifting feature detected from the phase differences. For the MP, as shown in the top-left panel of Fig. 7, the distributions of the amplitudes of MP\_I are more concentrated than those of other parts of the MP, indicating that the whole weak preceding component has the same modulation period. It also shows that the  $\sim 12P$  modulation of the MP comes mainly from the weak preceding component. The phase differences of MP\_I are concentrated at  $-180^\circ$ , meaning that the phase of MP\_I is offset with respect to that of the IP

by  $-180^\circ$ . The corresponding time delay is about  $0.5 P_3$  (or  $\sim 6 P$ ) between the modulation pattern of the MP\_I and the IP, which confirms the anti-correlation between pulse energies of the MP\_I and the IP.

The phase differences of the first two components of the MP (MP\_II) decrease. The difference is  $\sim -30^\circ$  for the central region of MP\_II, corresponding to a time delay of  $\sim 1 P$ . This results in the  $\sim 1 P$  delay in the modulation of MP\_II (the dashed line in Fig. 6). It is noticed that there is phase evolution between the MP\_I and MP\_II. Consequently, the cross-correlation between them and the IP changes from negative to positive. Moreover, this correlation change is accomplished in a few pulse bins (less than  $2^\circ$  in pulse phase), so there is almost no transition process. However, for other parts of the MP, the  $\sim 12 P$  modulation pattern is weak, and the phase is dispersedly distributed. We conclude that the phases with strong  $\sim 12 P$  modulation features in the IP and the MP are phase locked. The same phase-locked (delay) modulations were also detected in the observations of 2018 September 5.

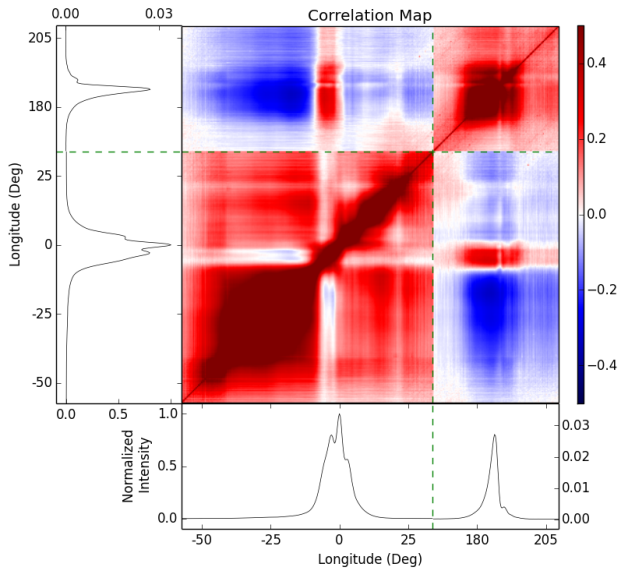


**Figure 5.** The longitude-longitude correlation between the MP and the IP for zero delay. The side and bottom windows show the mean pulse profile with intensity normalized to the peak of the MP. Longitudes between the MP and the IP (from  $34^\circ$  to  $164^\circ$ ) are deleted. The green dashed lines defined as the end longitude of the MP ( $34^\circ$ ) and the beginning longitude of the IP ( $164^\circ$ ).

### 3.3. The emission states and “bridge” emission

In this subsection, the emission modes are identified according to the periodic energy variation of the IP. Sin-

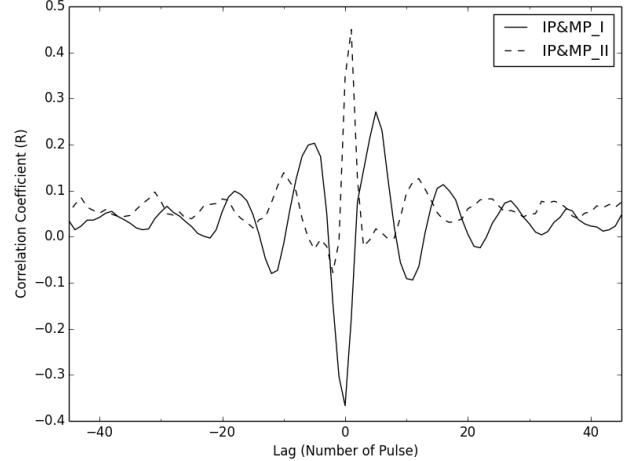


**Figure 6.** The cross-correlations between the pulse energies of the IP and other parts of the MP. The solid line is for the IP and the MP\_I, and dashed line is for the IP and the MP\_II.

gle pulses with on-pulse energy of the IP larger than  $3\sigma_{\text{IP,on}}$  are classified as strong-mode pulses. The others are weak-mode pulses, where  $\sigma_{\text{IP,on}}$  is the uncertainty of the on-pulse energy of the IP.  $\sigma_{\text{IP,on}} = \sqrt{N_{\text{on}}}\sigma_{\text{off}}$  is the uncertainty in the on pulse energy of the IP, where  $N_{\text{on}}$  is the number of on-pulse bins and  $\sigma_{\text{off}}$  is the rms of the off-pulse range (Bhattacharyya et al. 2010; Yan et al. 2019). The pulse energy sequence of the IP and the separated emission modes are given in Fig. 8. The number ratio of the strong mode pulse to the weak mode one is about 6 to 1. The polarization profiles for different states are shown in Fig. 9. The strong mode has a strong IP and weak preceding component of the MP, while the weak mode is the opposite. It is noticed that the interpulse-like structure is also visible in the weak mode, which implies that the periodic longitude intensity modulation is not periodic pulse nulling. A summary of the polarization parameters is given in table 1, where the mean total intensity  $I$ , the mean linear polarization intensity  $\langle L \rangle$  and the mean circular polarization intensity  $\langle |V| \rangle$  were all averaged over the on-pulse windows of the MP and the IP. As detected in previous studies (Rankin & Rathnasree 1997), PSR B1929+10 has high linear polarization, especially for the IP, whose linearly polarized intensity exceeds 90% of its total intensity. The fraction of the linear polarization and the circular polarization of the IP in the weak mode are higher than that in the strong mode. Due to the periodic modulation of MP\_II, the pulse width of the MP also show periodic changes. As reported in previous works, the polarization position angle shifts near the leading edge of the main pulse. This corresponds to a null in the linear polarized intensity,

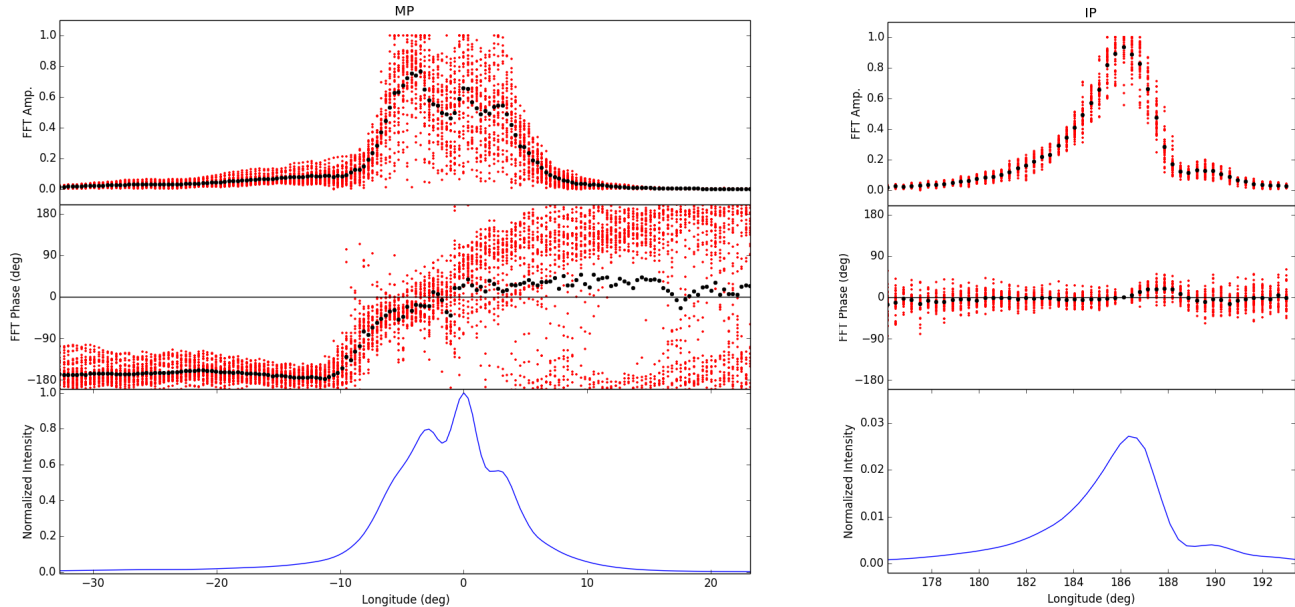


**Figure 7.** Variations of the LRFs across the pulse window for the MP (left column) and the IP (right column) of PSR B1929+10. The panels from top to bottom show the peak amplitudes, the corresponding phase variations and the normalized integrated pulse profiles. The peak amplitudes and the phases for each LRFs are shown as red points, while their average values are shown as black points.

which can be explained by a switch in two competing orthogonal emission modes (Stinebring et al. 1984).

By fitting the RVM to the position angle, a small inclination angle of  $\sim 35^\circ$  was found for PSR B1929+10 (Rankin & Rathnasree 1997). However, a relatively large inclination angle of  $61^\circ$  was given by Stairs et al. (1999). In this work, we have carried out an RVM fit to the PA swing using the program of PSRSALSA. The best RVM fit to the PA swing for the whole phase (with longitudes from  $-50^\circ$  to  $200^\circ$ ) shows that the inclination angle  $\alpha$  is  $145.3^\circ$  and the impact angle of the sight line is  $-20.2^\circ$  for the MP and  $91^\circ$  for the IP. The best fit has a reduced  $\chi^2 = 16628$ . We then only select the longitudes of the MP for the RVM fitting (with longitudes from  $-50^\circ$  to  $50^\circ$ ), the best fit  $\alpha$  and  $\beta$  are  $133.5^\circ$  and  $-24.0^\circ$  with reduced  $\chi^2 = 29.9$ . It is still not a good fit because the position angle swing contains many structures and deviates from the typical “S” shape. We will do further analysis on the single-pulse polarized features for such sources in the following work.

Weak emission following the MP (or preceding the IP) was clearly detected at 430 MHz by the Arecibo telescope, which was reported to have high fractional linear polarization just like the MP and the IP (Rankin & Rathnasree 1997). However, it was comparable to the noise level at 1414 MHz in previous studies. The weak emission following the MP is obviously detected in our data. In order to avoid being affected by random noise,

the observation was divided into several intervals in both time and frequency. Fig. 10 shows the integrated pulse profiles at different time and frequency intervals. In general, the low-level emission in pulse longitudes from  $70^\circ$  to  $165^\circ$  is visible in all of the individual data sets, like a “bridge” connecting the MP and the IP and called postcursor component (PC for short) in previous works (Lyne & Manchester 1988; Rankin & Rathnasree 1997). The fractional linear polarization of this component is almost  $\sim 100\%$ . We carried out fluctuation spectral analysis for the “bridge” emission, but there were no obvious modulation features found. However, there is no such “bridge” emission on the other side of the IP. As shown in the Fig. 10, its position is also independent of frequency.

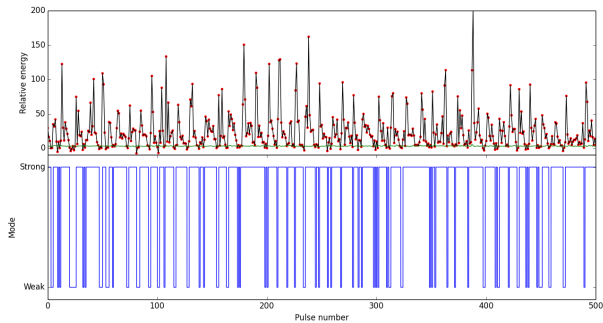
### 3.4. The pulse profile evolution with frequency

Many pulsars exhibit significant evolution in their pulse shapes with observing frequency. The changes in pulse width and separation between different components are generally taken to be a consequence of emission from different heights (Craft 1970; Cordes 1978). Some other changes such as relative intensity differences between components are usually related to the variation in geometry or the emission mechanism (Lorimer & Kramer 2004).

Fig. 11 presents the intensity ratio (top panel) and longitude separation (bottom panel) between the IP and the MP at different frequencies. The best linear fits for

**Table 1.** Polarization parameters of the IP and the MP for the mean pulse, the strong mode and the weak mode.

State	MP					IP				
	$W_{50}$ (Degree)	$W_{10}$ (Degree)	$\langle L \rangle / I$ (Percent)	$\langle V \rangle / I$ (Percent)	$\langle  V  \rangle / I$ (Percent)	$W_{50}$ (Degree)	$W_{10}$ (Degree)	$\langle L \rangle / I$ (Percent)	$\langle V \rangle / I$ (Percent)	$\langle  V  \rangle / I$ (Percent)
Mean	9.3	18.3	69	-1.3	2.4	3.3	10.9	92	-5.4	5.4
Strong State	9.3	17.9	70	-1.5	2.4	3.3	10.9	91	-5.3	5.3
Weak State	8.8	19.7	62	0.3	2.1	3.0	3.2	99	-11	13

**Figure 8.** The pulse energy sequence of the IP (upper panel) and the separated emission modes (bottom panel). The red points in the upper panel are the on-pulse energies of the IP and the green line is the  $3\sigma_{\text{off}}$  level of the off-pulse region for single pulses. Pulses with energy below the green line are classified as being in the weak mode, and others are taken as the strong mode.

the intensity ratio shows that the peak intensity ratio of the IP to the MP decreases as the frequency increases. However, the evolution trend is not clear because of the large measurement errors.

In the work of [Hankins & Fowler \(1986\)](#), a Gaussian curve was fitted to the weak IP, and the centroid was used as the IP fiducial point to measure its position from the peak of the MP. The separation between them was reported to be  $187.4 \pm 0.2^\circ$ , independent of frequency. However, the IP profile can be detected with high signal-to-noise ratio by the high-sensitivity observations of FAST, and the peaks of the IP and the MP were chosen to measure their separation in this paper. The errors are calculated based on the rms noise. The longitude separations between the IP and the MP at different frequencies are shown in the lower panel of [Fig. 11](#). It is  $186.3 \pm 0.3^\circ$  in our work. The separation is found to be independent of radio frequency, which is consistent with the results of [Hankins & Fowler \(1986\)](#).

## 4. DISCUSSION

### 4.1. The periodic amplitude modulation

The emission properties of PSR B1929+10 exhibit great complexity. The most significant feature is the periodic modulation in the IP and parts of the MP. The weak preceding component of the MP shows the same modulation period as the IP ([Fig. 4](#)). As shown in the left column of [Fig. 3](#), the fluctuation spectrum of

the MP shows a broad low-frequency structure with two relatively significant features at 0.1 cpp and 0.18 cpp, mainly from its first two components. We confirm that it is periodic amplitude modulation rather than subpulse drifting because there is no systematic drifting pattern detected in the data. Recently, periodic amplitude modulation has been detected in 19 radio pulsars ([Basu et al. 2020; Yan et al. 2020](#)). [Yan et al. \(2019\)](#) reported that the IP and the precursor of PSR B1822-09 are modulated with a period of  $\sim 43P$  in its quiet (Q) mode. Similar amplitude modulations were also found PSRs B1946+35, J1048-5832 and the burst(B) mode of PSR B0823+26 ([Mitra & Rankin 2017; Yan et al. 2020; Basu & Mitra 2019](#)). [Basu et al. \(2016, 2020\)](#) studied the known pulsars with periodic modulation (including systematic drifting and amplitude modulation), and found clear differences between pulsars with subpulse drifting and those with periodic amplitude modulation/nulling, which are shown in [Fig. 12](#). The subpulse drifting is only seen in pulsars with spin-down energy loss rate ( $\dot{E}$ ) below  $5 \times 10^{32}$  erg/s. However, periodic amplitude modulation can be seen in pulsars with relatively longer modulation period and larger spin-down energy loss rate, which implies that it has a distinct physical origin compared with subpulse drifting ([Basu et al. 2020](#)). PSR B1929+10 has a relatively large spin-down energy loss rate of  $\dot{E} \sim 3.93 \times 10^{33}$  erg/s, and modulation period  $\sim 12P$ . It lies in the group with periodic amplitude modulation (the red inverted triangle in [Fig. 12](#)).

Though there is no obvious boundary between the periodic amplitude modulation and periodic nulling, they are indeed different in their physical properties ([Basu et al. 2019a](#)). Similar to PSR B1822-09, there is no nulling pulse detected in the data of PSR B1929+10. We also made an on-pulse energy distribution for the IP, and found that the peak of on-pulse energy deviates from the zero point in the histogram, which confirmed that the periodic modulation of PSR B1929+10 is caused by emission mode switching.

### 4.2. The phase-locking features in other pulsars

The second remarkable feature in PSR B1929+10 is the phase-locked (delay) modulation between the IP and the MP. As analysed in subsection 3.2, the  $\sim 12P$  modulation pattern in the IP is correlated (or anti-correlated) with that in the components of the MP. The energy fluctuation

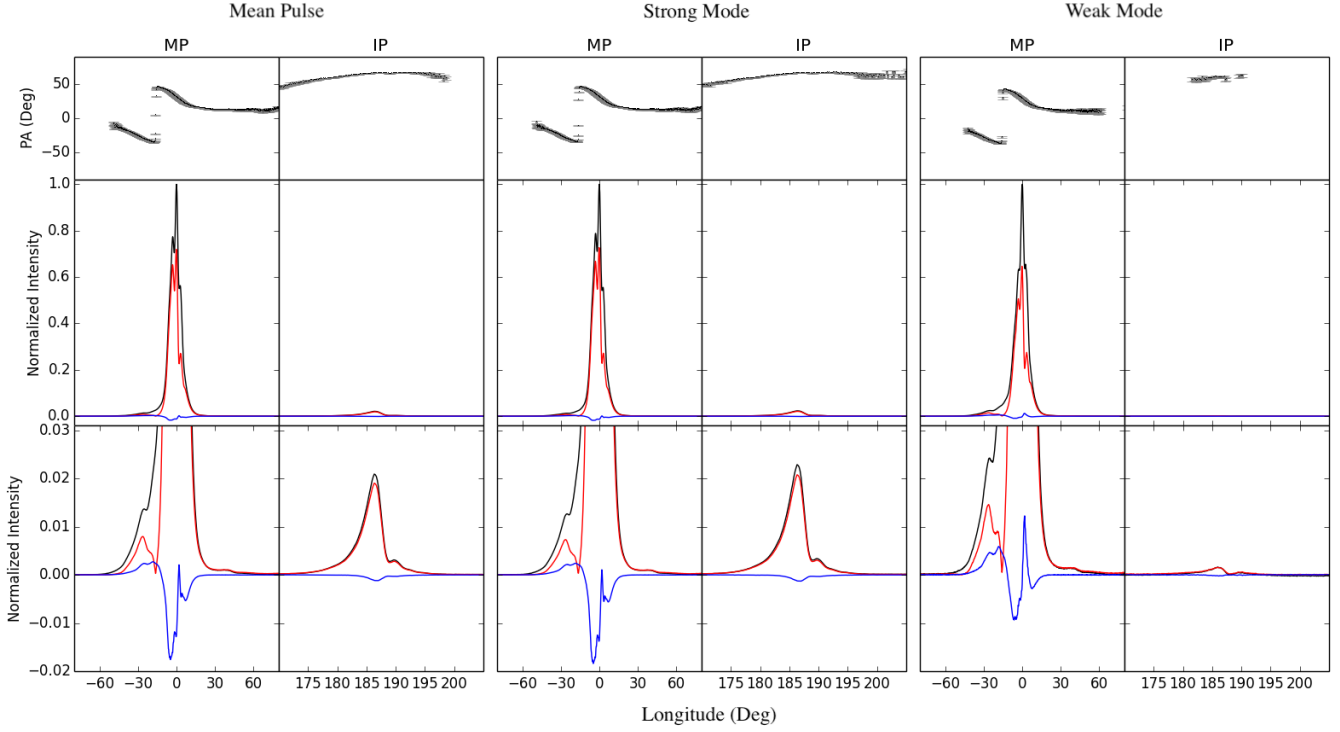


**Figure 9.** The polarized pulse profiles of PSR B1929+10 for the mean pulse (left), the strong mode (middle) and the weak mode (right) from the observation of 2019 November 22. The top panels show the position angles of the linearly polarized emission. The middle panels show the total intensity (black), the linearly polarized intensity (red) and the circularly polarized intensity (blue). The bottom panels are the expanded plots of the middle panels.

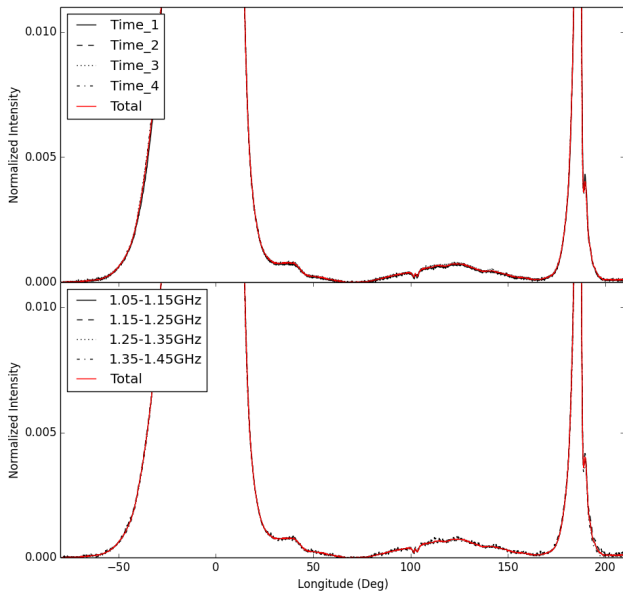


**Figure 10.** The integrated pulse profiles at different time and frequency intervals. The intensity is normalized to the peak intensity of the MP.

tuations in the IP and the weak preceding component of the MP are anti-correlated. However, it is positively correlated with that of the first two components of the MP. What is more interesting is that the modulation of MP<sub>II</sub> is delayed about  $1P$ . The phase-locked (delay) modulation is also detected in the observation on 2018 September 5. Combined with the periodic amplitude fluctuation reported by Basu et al. (2016), it is possible that the phase locking is a permanent feature for PSR B1929+10. It is puzzling that (1) there is a correlation transition from negative to positive on the leading edge of the MP, (2) there is a phase-locked (delay) between the IP and different parts of the MP.

Similar phase-locked (delay) modulation has been reported for PSRs B1702-19, B1055-52 and B1822-09 (Weltevrede et al. 2007, 2012; Yan et al. 2019). For PSR B1702-19, its IP and the trailing part of the MP are modulated with a period of  $\sim 10P$ , and are phase-locked by half-period delay (Weltevrede et al. 2007). Both the MP and the IP of PSR B1055-52 contain several emission components, and are modulated by a period of  $\sim 20P$ . Furthermore, the periodicity exhibits a phase-locked delay by  $2.5P$  between the MP and the IP (Weltevrede et al. 2012). For PSRs B1702-19 and B1055-52, both of their modulation patterns are positive corre-

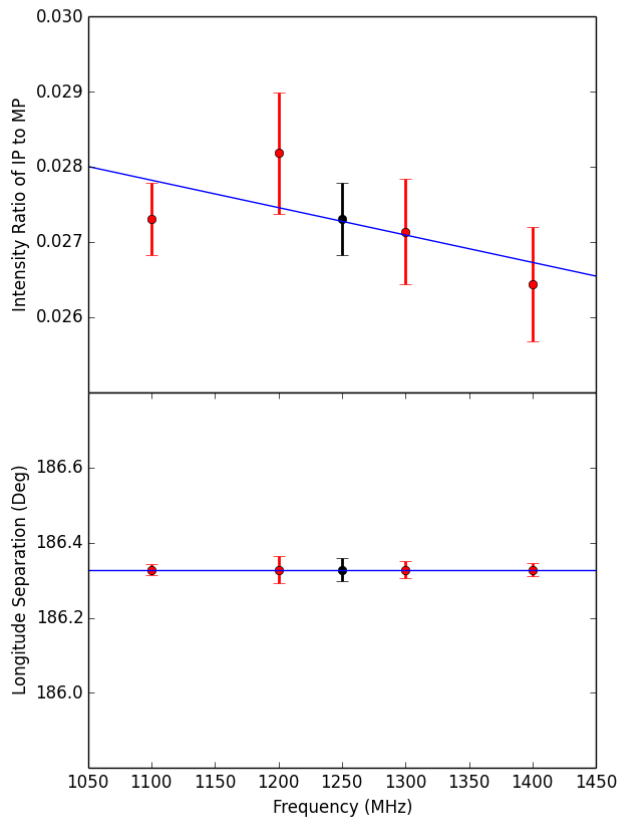


**Figure 11.** The intensity ratio (top panel) and longitude separation (bottom panel) between the IP and MP at different frequencies. The red points in each panel are the average values at the center frequencies of different frequency intervals, and the black points are those of all observing frequencies. The blue lines are best linear fits for the intensity ratio and the longitude separation as a function of frequency.

lated. PSR B1822-09 was reported to switch between its B-mode and Q-mode according to the appearance and disappearance of the precursor component. Meanwhile, the IP changes in the opposite way to the precursor component. The average time between mode changes was a few minutes (Yan et al. 2019). However, there was no phase-locked (delay) modulation reported between the precursor and the IP. A recent investigation revealed that the IP and the leading component of the MP were modulated with a period of  $\sim 43 P$  in the Q-mode (Yan et al. 2019). This periodic modulation was found to be phase-locked.

The modulation parameters of PSRs B1055-52, B1702-19, B1822-09 and B1929+10 are shown in Table 2. The comparison with other periodic modulation pulsars is shown in Fig. 12. It seems that pulsars with

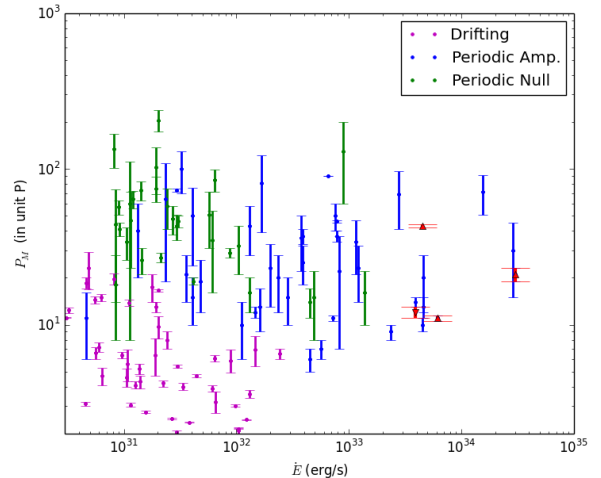


**Figure 12.** The modulation periods ( $P_M$ ) as a function of the spin-down energy loss ( $\dot{E}$ ) (Basu et al. 2017, 2019a, 2020). The magenta points are pulsars with subpulse drifting, the blue ones are for periodic amplitude modulation, and the green ones are for periodic nulling. PSRs B1055-52, B1702-19 and B1822-09 are labelled as red triangles, and PSR B1929+10 is labelled as red inverted triangle.

**Table 2.** The (modulation) parameters of PSRs B1055-52, B1702-19, B1822-09 and B1929+10.

PSRB	$P$	$\dot{P}$	$P_3$	$\dot{E}$	$P_{delay}$	$\tau_{delay}$
	$s$	$(10^{-15})$ $s/s$	$P$	$(10^{33})$ $erg/s$	$P$	$s$
1055-52	0.197	5.83	$21 \pm 2^a$	30	$2.5^a$	0.49
1702-19	0.299	4.14	$11 \pm 0.4^b$	6.1	$0.5^b$	0.15
1822-09	0.769	52.5	$43 \pm 1^c$	4.5	—	—
1929+10	0.227	1.16	$12 \pm 1$	3.9	1	0.23

a, (Weltevrede et al. 2007).

b, (Weltevrede et al. 2012).

c, (Yan et al. 2019).

phase-locked (delay) modulation have relatively larger energy loss rates.

For PSR J0826+2637, its MP and postcursor component also show periodic amplitude modulations in the B-mode. However, the IP is too weak to detect any modulation features (Basu & Mitra 2019). In addition to the periodic modulation in the intensity, the pulse width of single pulses also shows periodic changes at both the leading and trailing sides in its B-mode (Basu & Mitra 2019). Similar to PSR J0826+2637, the MP's pulse width of PSR B1929+10 also changes periodically at its leading side due to the intensity fluctuation of MP.II.

#### 4.3. The emission geometry for PSR B1929+10

Much efforts have gone into studying the emission mechanism and magnetospheric structure of the pul-

sar. It seems that the relatively small inclination angle has categorised PSR B1929+10 as a single-pole interpulsar. Furthermore, the weak “bridge” emission between the MP and the IP provides important evidence for the single-pole emission hypothesis (Manchester & Lyne 1977; Gil 1985). However, the single wide cone model of Manchester & Lyne (1977) is first ruled out in the case of PSR B1929+10, because of the frequency independence of the separation between the IP and the MP. In the single-pole scenario, Dyks et al. (2005) proposed a competing model to explain the anti-correlation between the energy fluctuation in the IP and the precursor component of PSR B1822-09. It assumes that there is an emission region close to the MP emission region, which changes its emission direction outward/inward towards the neutron star, and would be respectively observed as the precursor component and the IP as the pulsar rotates. This model suggests that the precursor component and the IP should have the same origin but outside the region of the MP. As discussed in subsection 4.2, while there are many observational similarities between PSRs B1822-09 and B1929+10, the anti-correlation between the weak preceding component of the MP and the IP could be understood in the same way. However, a separation of  $180^\circ$  between the anti-correlated components is expected in this model, which is obviously not the case for PSR B1929+10, a separation of  $211^\circ$  is measured between the IP and the weak preceding component. Weltevrede et al. (2007) discussed a possibility caused by retardation and aberration in a bidirectional model, which says that emission from higher would arrive earlier to the observer. According to this model, the emission height of the IP and MP\_I is expected to be 700 km if the minimum of the linear polarization between MP\_I and MP\_II is set to be the fiducial points (longitude of the magnetic pole on the star). The derived height of the MP is expected to be 850 km and its emission beam defined by the last closed fieldlines is  $24^\circ$ . Accordingly, the component width is expected to be  $42^\circ$  which is roughly consistent with the observed width of the MP.

The polarization profile of PSR B1929+10 has been studied in detail, showing that both the center of the MP and the IP have relatively higher circular polarization, which indicates that both the MP and the IP should be dominated by core emission (Rankin 1983; Rankin & Rathnasree 1997; Basu et al. 2015). By identifying the core components and calculating their widths from the MP and the IP regions, PSR B1929+10 has been taken as an orthogonal rotator since then. In the two-pole scenario, both poles of the pulsar are synchronously modulated with the same period of  $\sim 12P$ . Just like

PSR B1055-22 (Weltevrede et al. 2012), it seems that the MP of PSR B1929+10 imitates the IP in intensity and pattern. There must be information transmission from one pole to the other. Weltevrede et al. (2012) discussed possible physical mechanisms of neutron star nonradial oscillation, which provided a way to explain the interpole phase-locking via the neutron star surface. The positive correlation and the  $\sim 1P$  modulation delay between the IP and the MP\_II can be naturally explained in this model. However, we still need to explain the anti-correlation between the modulations in the IP and the weak preceding components of the MP.

Compared with postcursor and precursor components of other pulsars, the PC of PSR B1929+10 is the widest of all, being about  $\sim 96^\circ$ . It is fully linearly polarized and there is no modulation feature found in this component. Moreover, its position also stay constant with frequency (see the bottom panel of Fig. 10). Basu et al. (2015) summarized the pre/post-cursor emission of different pulsars, and demonstrated the pre/post-cursor should have an origin outside the region of the MP and have a different emission mechanism.

To sum up, the interaction between the radio emission from the MP and the IP is a conundrum for present pulsar theories, and has important implications for understanding the emission mechanism and structure of the pulsar magnetosphere. According to the emission properties, all 44 known interpulse emitting pulsars are classified into two groups: double-pole model and single-pole model (Maciesiak et al. 2011). Evidence for alignment of the magnetic axis with the rotational axis was found by comparing the characteristic ages of pulsars in these two groups (Maciesiak et al. 2011).

## 5. CONCLUSIONS

We have carried out a detailed single pulse analysis on PSR B1929+10 based on FAST observations. Our high sensitivity observation reveals that the weak IP shows clear pulse-to-pulse modulation. With the fluctuation spectrum analysis, we found that both the MP and IP are modulated by a period of  $\sim 12P$ , and confirmed that it is a periodic amplitude modulation because there are no obvious subpulse drifting features detected in our data. Due to the high time resolution possible with the FAST sensitivity, the components which contribute to the  $\sim 12P$  modulation could be well identified. Correlation studies revealed that the fluctuation in the IP is anti-correlated with that in the weak preceding component of the MP (MP\_I), but correlated with that in the first two components of the MP (MP\_II). We also found that the modulation in the first two components of the MP is delayed compared to that in the IP by about  $1P$ .

We classified the pulses as to being in strong and weak modes according to the periodic energy variation in the IP. The pulse profile shape of the MP also changes because parts of its components have the same modulation period as the IP. It is puzzling that the IP and the MP are phase locked. These facts imply that the magnetosphere should be modulated periodically and globally, and there should be transfer of information between different emission regions or poles.

Weak “bridge” emission between the IP and the MP is clearly detected at 1.25 GHz, which has been taken as important evidence favoring the single-pole model. However, the separation between the IP and the MP is confirmed to be independent of observing frequency, which rules out the single wide cone model in the single-pole scenario. Observations of PSR B1929+10 with FAST represent a conundrum for pulsar theories and cannot be satisfactorily explained by the current pulsar models. Much work still needs to be done to fully understand pulsar radio emission and the structure of neutron star magnetosphere.

## 6. ACKNOWLEDGEMENTS

We would like to thank the referee for the comments and suggestions which helped to improve the paper. This work is supported by the West Light Foundation of the Chinese Academy of Sciences (No. 2018-XBQNXZ-B-023), the National Key R&D Program of China un-

der grant number 2018YFA0404703, the Open Project Program of the Key Laboratory of FAST, NAOC, Chinese Academy of Sciences, the China Postdoctoral Science Foundation grant (2019M650847) and the Cultivation Project for FAST Scientific Payoff and Research Achievement of CAMS-CAS. WMY is supported by the 2021 open program of the Key Laboratory of Xinjiang Uygur Autonomous Region, the NSFC (Nos. U1831102, U1731238, U1838109, U11873080) and the CAS “Light of West China” Program (No. 2017-XBQNXZ-B-022). RY is supported by the West Light Foundation of the Chinese Academy of Sciences, project (No. 2016-QNXZ-B-24). YZY is supported by the Guizhou Education Department, grant (No. Qian Education Contract KY[2019]214). DL is supported by CAS Strategic Priority Research Program (No. XDB23000000). YLY is supported by the National Key R&D Program of China (2017YFA0402600) and the CAS “Light of West China” Program.

The FAST FELLOW-SHIP is supported by Special Funding for Advanced Users, financed and administered by the Center for Astronomical Mega-Science, Chinese Academy of Sciences (CAMS). This work made use of the data from FAST (Five-hundred-meter Aperture Spherical radio Telescope). FAST is a Chinese national mega-science facility, operated by the National Astronomical Observatories, Chinese Academy of Sciences.

## REFERENCES

- Backer, D. C. 1973, *ApJ*, 182, 245, doi: [10.1086/152134](https://doi.org/10.1086/152134)
- Basu, R., & Mitra, D. 2019, *MNRAS*, 487, 4536, doi: [10.1093/mnras/stz1590](https://doi.org/10.1093/mnras/stz1590)
- Basu, R., Mitra, D., & Melikidze, G. I. 2017, *ApJ*, 846, 109, doi: [10.3847/1538-4357/aa862d](https://doi.org/10.3847/1538-4357/aa862d)
- . 2020, *ApJ*, 889, 133, doi: [10.3847/1538-4357/ab63c9](https://doi.org/10.3847/1538-4357/ab63c9)
- Basu, R., Mitra, D., Melikidze, G. I., et al. 2016, *ApJ*, 833, 29, doi: [10.3847/1538-4357/833/1/29](https://doi.org/10.3847/1538-4357/833/1/29)
- Basu, R., Mitra, D., Melikidze, G. I., & Skrzypczak, A. 2019a, *MNRAS*, 482, 3757, doi: [10.1093/mnras/sty2846](https://doi.org/10.1093/mnras/sty2846)
- . 2019b, *MNRAS*, 482, 3757, doi: [10.1093/mnras/sty2846](https://doi.org/10.1093/mnras/sty2846)
- Basu, R., Mitra, D., & Rankin, J. M. 2015, *ApJ*, 798, 105, doi: [10.1088/0004-637X/798/2/105](https://doi.org/10.1088/0004-637X/798/2/105)
- Becker, W., Kramer, M., Jessner, A., et al. 2006, *ApJ*, 645, 1421, doi: [10.1086/504458](https://doi.org/10.1086/504458)
- Bhattacharyya, B., Gupta, Y., & Gil, J. 2010, *MNRAS*, 408, 407, doi: [10.1111/j.1365-2966.2010.17116.x](https://doi.org/10.1111/j.1365-2966.2010.17116.x)
- Cordes, J. M. 1978, *ApJ*, 222, 1006, doi: [10.1086/156218](https://doi.org/10.1086/156218)
- Craft, Harold Dumont, J. 1970, PhD thesis, CORNELL UNIVERSITY.
- Dyks, J., Zhang, B., & Gil, J. 2005, *ApJL*, 626, L45, doi: [10.1086/431651](https://doi.org/10.1086/431651)
- Edwards, R. T., & Stappers, B. W. 2002, *A&A*, 393, 733, doi: [10.1051/0004-6361:20021067](https://doi.org/10.1051/0004-6361:20021067)
- Gil, J. 1985, *ApJ*, 299, 154, doi: [10.1086/163688](https://doi.org/10.1086/163688)
- Hankins, T. H., & Fowler, L. A. 1986, *ApJ*, 304, 256, doi: [10.1086/164159](https://doi.org/10.1086/164159)
- Hotan, A. W., van Straten, W., & Manchester, R. N. 2004, *PASA*, 21, 302, doi: [10.1071/AS04022](https://doi.org/10.1071/AS04022)
- Jiang, P., Yue, Y., Gan, H., et al. 2019, *Science China Physics, Mechanics, and Astronomy*, 62, 959502, doi: [10.1007/s11433-018-9376-1](https://doi.org/10.1007/s11433-018-9376-1)
- Jiang, P., Tang, N.-Y., Hou, L.-G., et al. 2020, *Research in Astronomy and Astrophysics*, 20, 064, doi: [10.1088/1674-4527/20/5/64](https://doi.org/10.1088/1674-4527/20/5/64)
- Large, M. I., Vaughan, A. E., & Wielebinski, R. 1968, *Nature*, 220, 753, doi: [10.1038/220753a0](https://doi.org/10.1038/220753a0)
- Li, D., Wang, P., Qian, L., et al. 2018, *IEEE Microwave Magazine*, 19, 112, doi: [10.1109/MMM.2018.2802178](https://doi.org/10.1109/MMM.2018.2802178)

- Lorimer, D. R., & Kramer, M. 2004, *Handbook of Pulsar Astronomy*, Vol. 4
- Lyne, A. G., & Manchester, R. N. 1988, *MNRAS*, 234, 477, doi: [10.1093/mnras/234.3.477](https://doi.org/10.1093/mnras/234.3.477)
- Maciesiak, K., Gil, J., & Ribeiro, V. A. R. M. 2011, *MNRAS*, 414, 1314, doi: [10.1111/j.1365-2966.2011.18471.x](https://doi.org/10.1111/j.1365-2966.2011.18471.x)
- Manchester, R. N., Hobbs, G. B., Teoh, A., & Hobbs, M. 2005, *AJ*, 129, 1993, doi: [10.1086/428488](https://doi.org/10.1086/428488)
- Manchester, R. N., & Lyne, A. G. 1977, *MNRAS*, 181, 761, doi: [10.1093/mnras/181.4.761](https://doi.org/10.1093/mnras/181.4.761)
- Misanovic, Z., Pavlov, G. G., & Garmire, G. P. 2006, in *AAS/High Energy Astrophysics Division #9, AAS/High Energy Astrophysics Division*, 7.58
- Mitra, D., & Rankin, J. 2017, *MNRAS*, 468, 4601, doi: [10.1093/mnras/stx814](https://doi.org/10.1093/mnras/stx814)
- Nan, R., Li, D., Jin, C., et al. 2011, *International Journal of Modern Physics D*, 20, 989, doi: [10.1142/S0218271811019335](https://doi.org/10.1142/S0218271811019335)
- Perry, T. E., & Lyne, A. G. 1985, *MNRAS*, 212, 489, doi: [10.1093/mnras/212.2.489](https://doi.org/10.1093/mnras/212.2.489)
- Phillips, J. A. 1990, *ApJL*, 361, L57, doi: [10.1086/185826](https://doi.org/10.1086/185826)
- Rankin, J. M. 1983, *ApJ*, 274, 333, doi: [10.1086/161450](https://doi.org/10.1086/161450)
- Rankin, J. M., & Rathnasree, N. 1997, *Journal of Astrophysics and Astronomy*, 18, 91, doi: [10.1007/BF02714873](https://doi.org/10.1007/BF02714873)
- Stairs, I. H., Thorsett, S. E., & Camilo, F. 1999, *ApJS*, 123, 627, doi: [10.1086/313245](https://doi.org/10.1086/313245)
- Stinebring, D. R., Cordes, J. M., Rankin, J. M., Weisberg, J. M., & Boriakoff, V. 1984, *ApJS*, 55, 247, doi: [10.1086/190954](https://doi.org/10.1086/190954)
- van Straten, W., & Bailes, M. 2011, *PASA*, 28, 1, doi: [10.1071/AS10021](https://doi.org/10.1071/AS10021)
- van Straten, W., Manchester, R. N., Johnston, S., & Reynolds, J. E. 2010, *PASA*, 27, 104, doi: [10.1071/AS09084](https://doi.org/10.1071/AS09084)
- Weltevrede, P., Edwards, R. T., & Stappers, B. W. 2006, *A&A*, 445, 243, doi: [10.1051/0004-6361:20053088](https://doi.org/10.1051/0004-6361:20053088)
- Weltevrede, P., Wright, G., & Johnston, S. 2012, *MNRAS*, 424, 843, doi: [10.1111/j.1365-2966.2012.21207.x](https://doi.org/10.1111/j.1365-2966.2012.21207.x)
- Weltevrede, P., Wright, G. A. E., & Stappers, B. W. 2007, *A&A*, 467, 1163, doi: [10.1051/0004-6361:20066957](https://doi.org/10.1051/0004-6361:20066957)
- Yan, W. M., Manchester, R. N., Wang, N., et al. 2020, *MNRAS*, 491, 4634, doi: [10.1093/mnras/stz3399](https://doi.org/10.1093/mnras/stz3399)
- . 2019, *MNRAS*, 485, 3241, doi: [10.1093/mnras/stz650](https://doi.org/10.1093/mnras/stz650)